**JM** RAPIDS

# Nonlinear transition mechanism on a blunt cone at Mach 6: oblique breakdown

**Andrew B. Hartman[1],†, Christoph Hader[1] and Hermann F. Fasel[1]**

[1]Department of Aerospace and Mechanical Engineering, University of Arizona, Tucson, AZ 85721, USA

Direct numerical simulations (DNS) were carried out to investigate laminar-turbulent transition for a blunt (right) cone ($7°$ half-angle) at Mach 5.9 and zero angle of attack. First, (linear) stability calculations were carried out by employing a high-order Navier–Stokes solver and using very small disturbance amplitudes in order to capture the linear disturbance development. Contrary to standard linear stability theory (LST) results, these investigations revealed a strong 'linear' instability in the entropy-layer region for a very short downstream distance for oblique disturbance waves with spatial growth rates far exceeding those of second-mode disturbances. This linear instability behaviour was not captured with conventional LST and/or the parabolized stability equations (PSE). Secondly, a nonlinear breakdown simulation was performed using high-fidelity DNS. The DNS results showed that linearly unstable oblique disturbance waves, when excited with large enough amplitudes, lead to a rapid breakdown and complete laminar-turbulent transition in the entropy layer just upstream of the second-mode instability region.

**Key words:** high-speed flow, boundary layer stability, transition to turbulence

## 1. Introduction

The understanding of laminar-turbulent transition for hypersonic boundary layers is still far behind that of low-speed (incompressible) flows. Most of the current understanding of high-speed transition is on the early onset that is governed by linear stability theory (LST, Mack 1969). Very limited insight is available for the nonlinear transition region, which can cover a significant part of the downstream transition process (see for example Laible, Mayer & Fasel 2009; Marineau *et al.* 2014; Hader & Fasel 2019).

Particularly elusive has been the transition process in the nose region of blunted cones. This topic is often referred to in the literature in connection with 'transition reversal' (see for example Stetson 1979, 1983). Stetson found that the instability process in the entropy layer in the nose region of blunted cones plays a key role in the early (upstream)

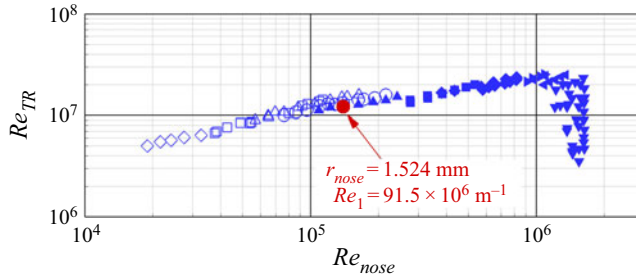† Email address for correspondence: andrewmach1@arizona.edu

Figure 1. Transition Reynolds number ($Re_{TR}$) vs nose-tip Reynolds number ($Re_{nose}$) based on the nose radius ($r_{nose}$); reproduced from Jewell & Kimmel (2016); (●, red) case considered in this paper and $Re_1$ is the unit Reynolds number used for the numerical investigations.

transition in conventional ('noisy') wind tunnels and that the transition Reynolds number consistently increases with nose bluntness, until a critical value is reached beyond which the transition Reynolds number abruptly decreases (figure 1), which he called 'transition reversal'. However, even for smaller nose radii, before transition reversal, he observed that transition was caused not by second-mode disturbances, but rather by a growth of disturbances in the entropy-layer region ('entropy-layer instability').

Subsequent theoretical investigations of the effect of nose bluntness for right cones using LST (see for example Dietz & Hein 1999; Lei & Zhong 2012; Rosenboom, Hein & Dallmann 2013) revealed that increasing nose bluntness monotonically shifts the critical Reynolds number (and consequently the transition location) further downstream, no matter how large the nose radius is. Thus, transition reversal could not be captured by LST.

More recently, Jewell *et al.* (2018) repeated the experiments by Stetson (1983) in the same tunnel for a right cone with a 7° opening half-angle, and also carried out stability calculations using the STABL parabolized stability equations (PSE) code (Jewell & Kimmel 2016; Jewell *et al.* 2018). They confirmed all of the relevant findings of the original experiments by Stetson (1983), and, more importantly, showed that PSE also did not provide any trend towards capturing transition reversal and/or indicate that the entropy-layer instability is playing an important role. Paredes, Choudhari & Li (2019*a*); Paredes *et al.* (2019*b*) suggested that considering non-modal disturbances, instead of modal, may explain the transition onset in the entropy layer as observed in experiments of Stetson (1983) and in the recent experiments by Kennedy *et al.* (2019). Paredes *et al.* (2019*a*,*b*) found larger *N*-factors (integrated growth rates) for the non-modal disturbances than were obtained by conventional modal (normal mode) stability analyses. However, these studies provided no conclusive evidence that non-modal analyses could explain entropy-layer transition, as even non-modal *N*-factors did not reach sufficiently large values to lead to transition.

The investigations discussed in the present paper are based on the assumption that considering the nonlinear disturbance development may be key for explaining the entropy-layer transition that has been observed in experiments. From numerous past investigations of hypersonic transition using DNS, we found that in addition to considering the 'linear' modal disturbance development, including the nonlinear effects, is crucially important for capturing the relevant transition mechanisms in high-speed wind tunnel experiments (see for example Laible *et al.* 2009; Hader & Fasel 2019).

Therefore, in the investigations of entropy-layer transition discussed in this paper, we have focused on the nonlinear disturbance development for a cone with a moderate nose bluntness. Of the classical candidates of nonlinear mechanisms (fundamental,
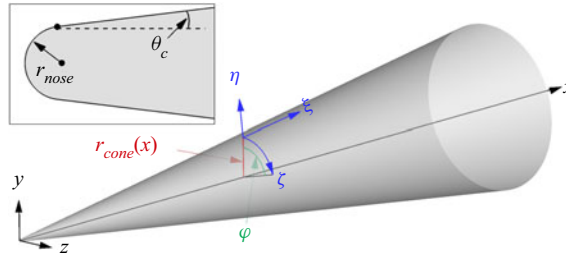
Figure 2. Schematic of the blunt-cone geometry.

subharmonic, oblique), emphasis was placed on the so-called 'oblique breakdown' discovered by Fasel, Thumm & Bestek (1993) for a Mach 1.6 flat-plate boundary layer, which was confirmed using nonlinear PSE by Chang & Malik (1994). This nonlinear breakdown mechanism was later found to also be relevant for a straight cone at Mach 3.5 (Laible *et al.* 2009) and a flat plate at Mach 3 (Mayer, Von Terzi & Fasel 2011*a*).

Wind-tunnel experiments (Stetson 1983; Kennedy *et al.* 2019) have shown that for blunted cones entropy-layer transition, and in particular transition reversal, occurs within a relatively short downstream extent close to the nose region. From our previous investigations, we have learned that oblique breakdown is an extremely rapid and powerful nonlinear mechanism that can lead to transition over a very short downstream distance (Fasel *et al.* 1993; Laible *et al.* 2009; Mayer *et al.* 2011*a*; Mayer, Wernz & Fasel 2011*b*), in fact, much more rapidly than for fundamental or subharmonic resonance. Furthermore, preliminary stability investigations using 'linear' DNS (with small amplitude disturbances) showed amplification only for oblique disturbances (see § 5). Therefore, oblique breakdown (with respect to entropy-layer instability) was an obvious candidate to be considered first for investigating the possible role of nonlinear effects on entropy-layer transition. For the results discussed in the present paper, the same case from the Air Force Research Laboratory (AFRL) experiments (Jewell *et al.* 2018) was chosen that was also investigated by Paredes *et al.* (2019*a*,*b*) using their non-modal analysis, based on which they concluded that non-modal (as opposed to modal) instabilities may be the key to understanding the transition process observed in the experiments.

In the present paper, results are also presented for the linear regime. However, the linear stability results were obtained using DNS rather than traditional LST or PSE. For the DNS stability investigations, extremely small disturbance amplitudes are used, so that the nonlinear effects become negligible. Thus, all of the so-called 'non-parallel flow effects' are included in the DNS and no assumptions regarding the disturbance form are required. It should be noted that the boundary layer in the nose region is strongly non-parallel due to the entropy-layer formation in that region.

## 2. Geometry and flow conditions

For the numerical investigation presented here, the geometry and the flow conditions of the experiments at the AFRL Mach 6 High-Reynolds Number Facility were used (Jewell *et al.* 2018). The geometry (see figure 2) is a $7°$ half-angle straight (right) cone with a nose radius of $r_{nose} = 1.524$ mm (0.06 in) corresponding to the 3 % bluntness case from Jewell *et al.* (2018). The flow conditions are summarized in table 1, and the case chosen is marked in figure 1 with a red dot. The fluid is considered to be a perfect gas with a constant Prandtl

| Parameter | Value |
|---|---|
| Stagnation pressure, $p_0$ | 2105 psi |
| Stagnation temperature, $T_0$ | 611 K |
| Mach number, $M$ | 5.9 |
| Unit Reynolds number, $Re_1$ | $91.5 \times 10^6$ m$^{-1}$ |

Table 1. Flow conditions.

number ($Pr = 0.71$) and a constant ratio of specific heats ($\gamma = 1.4$), and the viscosity is calculated using the standard Sutherland's law (no low-temperature correction).

## 3. Simulation strategy

For the simulations presented here, a three-step strategy was employed that has been successfully used previously for stability investigations and 'controlled' breakdown DNS for different geometries and flow conditions (see for example Laible *et al.* 2009; Hader & Fasel 2019). Step 1 consists of a precursor calculation to obtain the steady base flow around the entire geometry (including the nose) using either a finite-volume code developed in our CFD laboratory by Gross & Fasel (2008) or CFD++ (Chakravarthy *et al.* 1998). In step 2, a new base flow is calculated in a smaller subdomain using a high-order-accurate finite-difference code, which was also developed in our laboratory by Laible *et al.* (2009). In step 3, the actual stability and transition simulations are carried out in the same subdomain as for step 2 using the same high-order finite-difference code.

## 4. Base flow

Contours of Mach number and the density of the laminar base flow (figure 3) show the formation of a bow shock around the nose of the cone, resulting in a strong entropy layer. The inset in figure 3 indicates the entire size of the cone geometry as used in the experiments of Jewell & Kimmel (2016). The area shaded with dark grey in figure 3 highlights the extent of the subdomain used for the stability and transition simulations presented here. A comparison of the boundary-layer thickness determined at the location where the total enthalpy reaches 99.5 % of the total free stream enthalpy ($h_t(\delta_{99.5}) = 0.995h_{t\infty}$) and the entropy-layer thickness ($\delta_S$) calculated using ($\Delta S(\delta_S) = 0.25\Delta S_{wall}$, $\Delta S = c_p ln(T/T_\infty) - R_g ln(p/p_\infty)$ where $c_p$ and $R_g$ are the specific heat and gas constant of the fluid, respectively), as also used by Paredes *et al.* (2019*b*), is shown in figure 4. Close to the nose, the entropy layer is very thick compared with the boundary layer. The entropy-layer thickness rapidly decreases in the downstream direction but is not 'swallowed'. The edge Mach number ($M_e$ see figure 4) is drastically reduced compared with free stream Mach number due to the strong shock. For the entire computational domain, it remains well below $M_e = 4$.

## 5. Linear and nonlinear stability investigations

### 5.1. *Linear stability investigations*

For a blunt flat plate at $M = 2.5$, Dietz & Hein (1999) found amplified entropy-layer instabilities. Results from a LST analysis using our in-house developed linear stability solver (parallel flow assumptions, Haas 2020) for the geometry and flow conditions

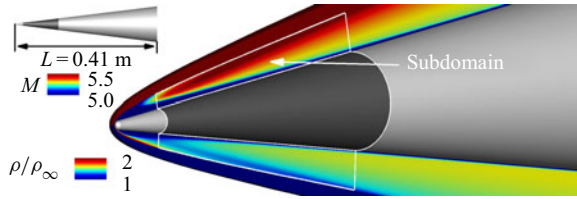Figure 3. Contours of Mach number ($M$) and density ($\rho$) normalized with the free-stream density ($\rho_\infty$), and the cone geometry as used in the original experiments with the dark grey shaded area highlighting the size of the computational domain used here.
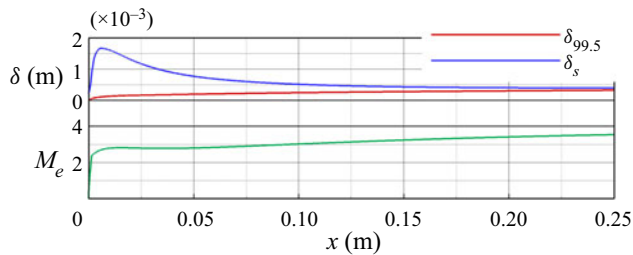


Figure 4. Development of the boundary layer and entropy-layer thickness ($\delta$), and the edge Mach number in the downstream direction.

considered here (table 1) are shown in figure 5. The location of the inflow and outflow boundaries of the computational domain that was used for the highly resolved 'controlled' breakdown DNS are highlighted in figure 5. No unstable disturbance waves in the computational domain considered here were found from the LST analysis. Note that in the same region unstable disturbance waves were also not found in the PSE analysis by Jewell *et al.* (2018). Therefore, 'linear' stability investigations were carried using DNS introducing small amplitude disturbances into the computational domain. Simulations by Husmeier & Fasel (2007) showed that for a blunt cone at $M = 8$ the flow field was most receptive to continuously forced disturbances in the entropy layer. Thus, for this 'linear' stability investigation, total energy perturbations were introduced into the entropy layer using a volume-forcing approach. Low resolution (in the azimuthal direction) calculations were carried out for a wide range of frequencies and azimuthal wavenumbers. The spatial growth rates extracted from these calculations are provided in figure 6(*a*). Close to the inflow of the computational domain, a region of substantial growth over a very short downstream distance for oblique waves ($k_c > 0$) of all the frequencies considered here can be observed (figure 6*a*). This very large linear growth was neither captured with LST nor with PSE, likely due to the assumptions required in LST and PSE. The maximum growth rates were obtained for an azimuthal wavenumber of $k_c \approx 300$. Due to the large growth rates of these unstable disturbances, relatively large $N$-factors (up to approximately 20) are reached over a short downstream distance as can be observed in figure 6(*b*). The 'linear' results clearly indicate that only oblique waves are amplified, while the flow is stable for axisymmetric waves (figure 6).

## 5.2. *Nonlinear stability investigations*

The linear stability investigations have shown that oblique disturbances are amplified while axisymmetric ones are not. Therefore, fundamental or subharmonic resonance are likely
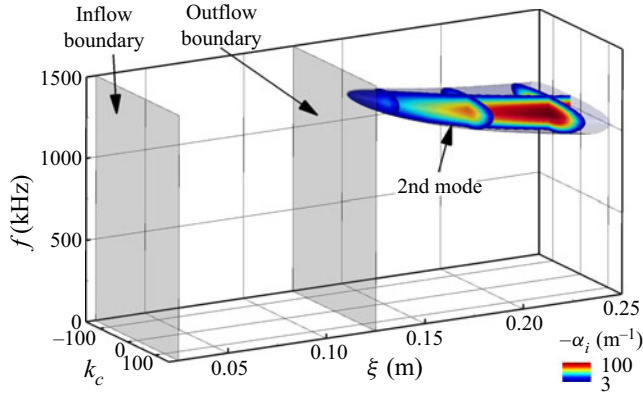
Figure 5. Growth rates from LST (A. Haas, private communication) for a wide range of frequencies ($f$) and azimuthal wavenumbers ($k_c$). The grey planes indicate the location of the inflow and outflow boundary of the computational domain used for the highly resolved DNS.
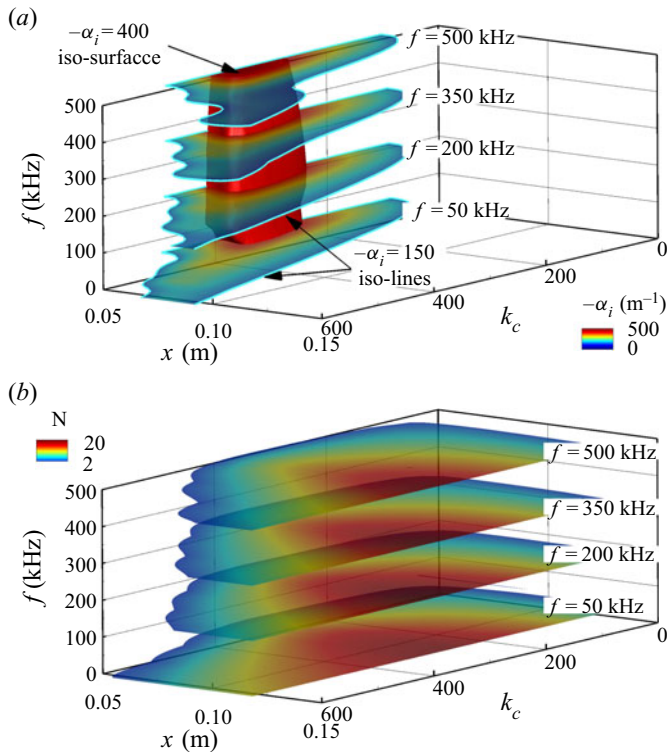


Figure 6. (*a*) Growth rates and (*b*) $N$-factors from 'linear' stability investigations using low amplitude DNS for a wide range of forcing frequencies and azimuthal wavenumbers with slices of constant frequency at $f = 50$, $f = 200$, $f = 350$ and $f = 500$ kHz.

not relevant in the computational domain considered here and for these flow conditions and nose bluntness. Consequently, the possibility of an oblique breakdown (Fasel *et al.* 1993) was investigated in detail. To allow for a possible future comparison with numerical investigations of the same geometry and flow conditions by Paredes *et al.* (2019*a*,*b*), a
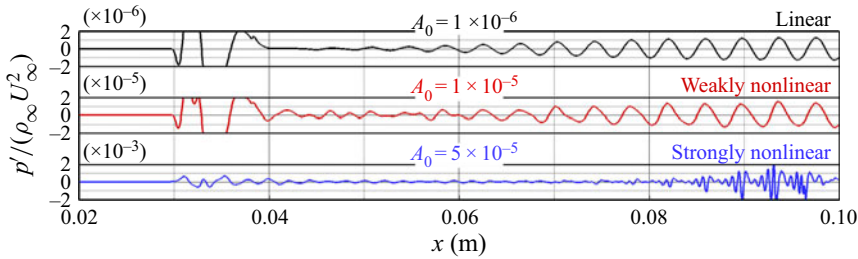
**915** R2-6

Figure 7. Instantaneous pressure disturbances ($p'$) normalized with twice the dynamic pressure, where $U_\infty$ is the freestream velocity, at the wall for three different forcing amplitudes ($A_0$).

pair of oblique disturbance waves with $f = 250$ kHz and an azimuthal wavenumber of $k_c = 50$ was chosen. This disturbance wave was found to have large linear amplification rates (see figure 6) in our stability investigations using DNS. While Paredes *et al.* (2019*a,b*) investigated the possibility of non-modal growth leading to transition, the very large linear amplification rates obtained from DNS are exploited here to rapidly trigger nonlinear interactions and a subsequent oblique breakdown. In order to find out if oblique breakdown can be initiated with the selected disturbance waves, an oblique breakdown onset study was carried out by forcing a pair of oblique disturbance waves ($f = 250$ kHz, $k_c = \pm 50$) with successively increasing amplitudes. The instantaneous pressure disturbances on the surface of the cone in figure 7 show that for a forcing amplitude of $A_0 = 1 \times 10^{-6}$ (figure 7, top) the disturbances are amplified after reaching the wall and the sinusoidal nature of the disturbances suggests that this is a purely 'linear' amplification. Increasing the forcing amplitude to $A_0 = 1 \times 10^{-5}$ (figure 7, middle) results in a distortion of the sinusoidal waveform of the instantaneous disturbance signal that is caused by nonlinear effects. When forced with a sufficiently large amplitude ($A_0 = 5 \times 10^{-5}$), a strong nonlinear distortion of the disturbance signal can be observed. This suggests that an oblique breakdown (Fasel *et al.* 1993) may be a relevant nonlinear mechanism.

## 6. Oblique breakdown

In the simulation set-up for the nonlinear transition investigation by Paredes *et al.* (2019*b*), non-modal disturbances (obtained from linear non-modal analysis, and 'blown-up' to large 'nonlinear' amplitudes) are forced at the inflow boundary of their computational domain. Thus, the nonlinear development resulting from that particular forcing is specific to what is imposed at the inflow as a boundary condition, in their case, a pair of non-modal oblique disturbances with $k_c = 50$, $f = 250$ kHz (Note that in Paredes *et al.* (2019*b*) the azimuthal wavenumber is denoted with *m*). In contrast, our simulation set-up was motivated by the landmark 'controlled' boundary-layer transition experiments by Schubauer & Skramstad (1948), which validated the LST for the primary instability. Furthermore, it is motivated by the subsequent 'controlled' transition experiments by Klebanoff, Tidstrom & Sargent (1962), which set the stage for the development of the secondary instability theory for incompressible boundary layers. In these experiments, local but 'controlled disturbances' of specified frequencies and amplitudes were introduced (via a 'vibrating ribbon'). Thus, in these landmark experiments, the receptivity of the flow with respect to the 'actuator' (vibrating ribbon) was included in the flow response. These 'controlled' transition experiments laid the foundation for the understanding of low-speed boundary-layer transition.

The simulations discussed in our paper are set up in the spirit of these landmark low-speed 'controlled' transition experiments as hypersonic experimental equivalents have not yet been carried out. Towards this end, in our simulations, the disturbances are deliberately not forced at the inflow, but rather, as in the above mentioned experiments, locally (in our case in the entropy layer) using 'controlled disturbances' (with respect to amplitude, frequency and azimuthal wavenumber), so that the 'actuator' receptivity to the employed forcing is also included. Therefore, the resulting nonlinear transition mechanisms are not driven by imposed streamwise modes at the inflow boundary as in Paredes *et al.* (2019*b*), but rather, the oblique transition mechanisms are allowed to 'play out freely' without any bias, and the streamwise modes are nonlinearly generated and can participate in the nonlinear transition process. It should be noted that a local 'controlled' disturbance generation as used in the present simulations could be realized in future high-speed transition experiments.

With the forcing parameters determined as discussed above, a highly resolved so-called 'controlled' oblique breakdown DNS was carried out. Towards this end, a pair of oblique disturbance waves with a frequency of $f = 250$ kHz and an azimuthal wavenumber of $k_c = \pm 50$ were introduced into the entropy layer with an amplitude of $A_0 = 5 \times 10^{-5}$. The computational domain for this simulation was focused on a region close to the blunted nose of the cone geometry (see figure 3). In the streamwise direction, the computational domain was resolved with $n_x = 6800$ grid points with the inflow boundary located at $x = 0.025$ m and the outflow at $x = 0.125$ m. The grid spacing was refined in the downstream direction in order to resolve all relevant length scales near the downstream end of the domain where the nonlinear breakdown stages will be reached. The shock-fitted grid extends up to the shock location which was obtained from precursor calculations. A total of $n_\eta = 698$ grid points clustered near the wall and in the entropy layer were used in the wall-normal direction. The computational domain in the azimuthal direction ($0$ rad $\leq \varphi \leq \pi/50$ rad) was resolved with $n_\varphi = 199$ grid points (100 Fourier modes). For the wall-normal direction, grid convergence studies were carried (not presented here for brevity) to ensure that the boundary layer and the entropy layer were sufficiently resolved. An *a priori* estimate of the wall units was obtained with the turbulent skin-friction estimates (White 2006). Based on these estimates, the grid line distribution was designed such that in the wall-normal direction $\Delta y^+ \approx 1$ was obtained in the entire computational domain, and $\Delta x^+ < 5$ was used in the refined region in the downstream direction where nonlinear breakdown was expected based on the oblique breakdown onset calculations (see § 5).

Contours of the instantaneous temperature disturbance in the symmetry plane from the nonlinear oblique breakdown DNS are shown in figure 8. For reference, the entropy-layer ($\delta_S$) and boundary-layer ($\delta_{99.5}$) thicknesses of the laminar base flow are also provided in figure 8. The oblique disturbance waves initially propagate along the entropy layer (figure 8*a*). The spatial forcing function used for the volume force was a so-called 'monopole' in the streamwise and the wall-normal direction. This shape is initially 'imprinted' on the disturbance waves but shortly downstream of the forcing location the disturbance waves adjust and exhibit an elongated shape 'slanted' upwards (figure 8*a*). A detailed view of the entropy-layer structures downstream of the forcing location (figure 8*b*) shows that the main structures are developing above the boundary layer. The 'tails' of these structures begin to penetrate the boundary layer (figure 8*b*) and then quickly become stretched in the streamwise direction due to the reduced flow speed inside of the boundary layer (figure 8*c*). While the structures comprising positive temperature disturbance values remain nearly unchanged, the structures that penetrated into the boundary layer (negative
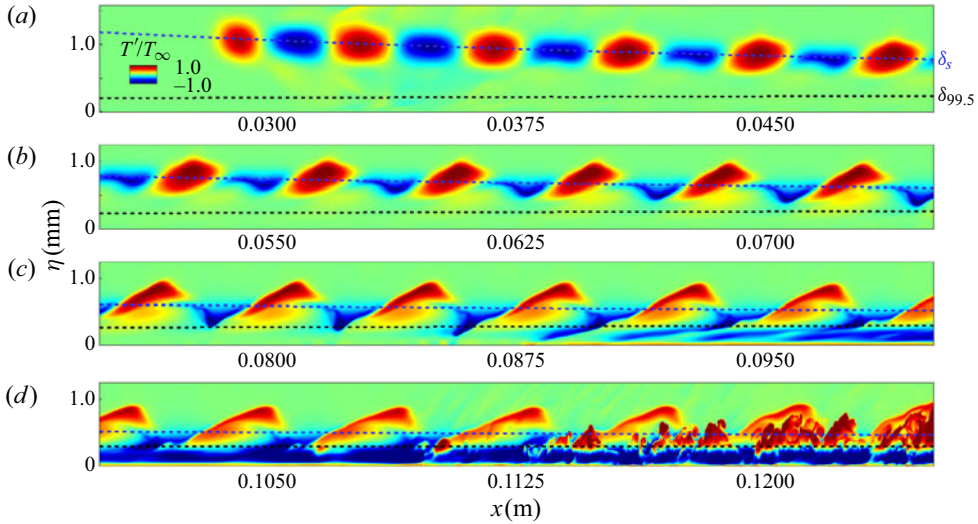
Figure 8. Contours of the instantaneous temperature disturbance ($T'$) normalized with the free-stream temperature ($T_\infty$) in the symmetry plane.
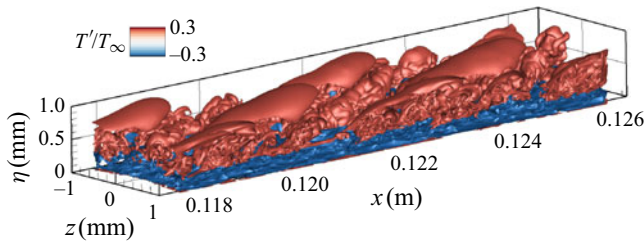


Figure 9. Isosurfaces of the instantaneous three-dimensional temperature disturbances in the turbulent breakdown region.

temperature disturbances) quickly merge and contaminate the entire boundary layer (figure 8d). Farther downstream, the 'tail' of the large structures in the entropy layer descends into the boundary layer and smaller scales are generated (figure 8d), indicating that the flow is progressing deeper into the nonlinear breakdown regime. Towards the end of the computational domain, the flow exhibits a breakdown to very small structures that are characteristic for a turbulent boundary layer. Remnants of the entropy-layer structures can still be observed even long after the nonlinear stages of the laminar-turbulent transition process have been reached. Thus, these 'coherent' structures persist far into the late stages of the transition process and into the turbulent boundary layer. The instantaneous three-dimensional structures of the late stages of the nonlinear transition process in figure 9 confirm that the coherent structures in the entropy layer prevail downstream into the late nonlinear transition stages. The negative temperature disturbances are layered between the wall and the positive temperature disturbances in the entropy layer.

The downstream development of the pressure disturbance amplitude extracted at the wall (figure 10a) and the maximum pressure disturbance amplitude (figure 10b) provide insight into which nonlinear interactions are dominating the transition process. For convenience, the notation $(n, m)$ which is a shorthand notation for $(n \times f_{forced}, m \times k_{c,domain})$, where $f_{forced}$ is the frequency of the forced disturbance wave and $k_{c,domain}$ is the smallest
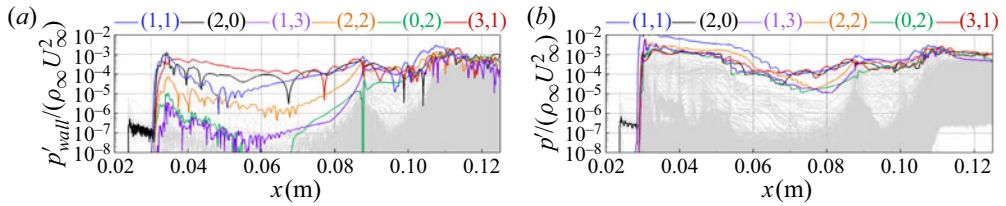
Figure 10. Downstream development of the pressure disturbance amplitude at the wall ($p'_{wall}$) (*a*), and the maximum pressure disturbance amplitude (*b*).

azimuthal wavenumber resolved in the computational domain has been adopted here (for details see Hader & Fasel 2019). For the results presented here, the normalization parameters are $f_{forced} = 250$ kHz and $k_{c,domain} = 50$. The development of the pressure disturbance amplitude at the wall (figure 10*a*) indicates that initially all modes are decaying downstream of the forcing location until a strong exponential (linear in the log plot) growth sets in, quickly leading to very large amplitudes for a wide range of disturbance waves at $x \approx 0.087$. Thereupon the oblique forced mode $(1, 1)$ and all nonlinearly generated modes reach peak values. Thereafter, surprisingly, the disturbances decay until $x \approx 0.095$ m, from whereon all disturbance waves experience strong amplification, in particular the higher frequencies and azimuthal wavenumbers (indicated with grey lines, figure 10). The modes highlighted in colour (figure 10) are the so-called 'signature modes' of the oblique breakdown (Fasel *et al.* 1993), thus providing evidence that oblique breakdown is indeed the dominant nonlinear mechanism. These observations are the same for the development of the maximum pressure disturbance amplitudes (figure 10*b*). The most notable difference is that the amplification of the forced mode $(1, 1)$ at the wall (figure 10*a*) sets in farther upstream (at approximately $x \approx 0.05$ m) compared with the development of the maximum pressure disturbance amplitude (at approximately $x \approx 0.07$ m, figure 10*b*).

As can be observed in figure 10(*b*), the streamwise mode $(0,2)$, as well as the other signature modes of oblique breakdown, are generated as a consequence of a nonlinear interaction of the oblique modes $(1,1)$ and $(1,-1)$ which are the only 'controlled' disturbances introduced into the flow due to the simulation set-up as discussed above. This is in contrast to the numerical investigations of Paredes *et al.* (2019*b*), where the streamwise modes were already introduced at the inflow of the computational domain by using disturbances obtained from a non-modal stability calculation.

The azimuthal wavenumber of the forced oblique waves was $k_c = 50$, resulting in a steady streamwise mode $(0, 2)$ with $k_c = 100$. In the non-modal analysis by Paredes *et al.* (2019*b*), a steady streamwise mode with $k_c = 100$ exhibits the largest *N*-factor. In the DNS for the 'controlled' oblique breakdown, not only steady streamwise modes but also a wide range of other modes are nonlinearly generated, in particular also the so-called 'signature modes' (see figure 10), which in turn can lead to other levels of nonlinear interactions. Therefore, it is difficult to establish an unambiguous link between the nonlinearly generated steady streamwise modes observed in the present oblique breakdown DNS and the steady streamwise modes obtained from the transient growth analysis by Paredes *et al.* (2019*b*). Our simulations seem to indicate that the nonlinear breakdown is not only associated with the secondary instability of the steady streamwise modes, as described by Berlin, Lundbladh & Henningson (1994) for incompressible flows, but is rather also caused by the rapid and strong nonlinear interactions with all the other unsteady, nonlinearly generated disturbances (see figure 10).
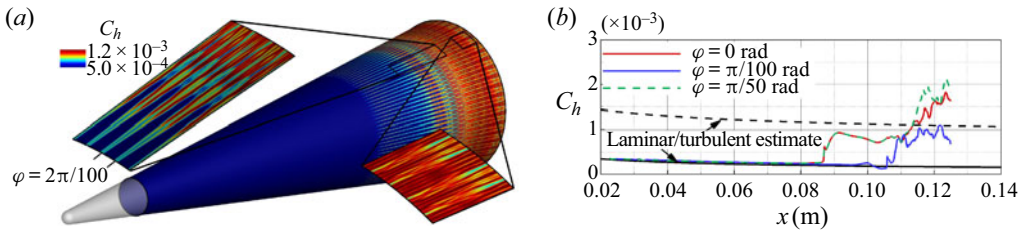
Figure 11. Contours of the time-averaged Stanton number ($C_h$) on the surface of the cone (*a*), and development of the Stanton number in the downstream direction (*b*).

Contours of the time-averaged Stanton number on the surface of the cone are displayed in figure 11(*a*). Towards the end of the computational domain, streaks of increased Stanton number ('hot streaks') begin to develop. The streak spacing in the azimuthal direction is $\Delta\varphi = 2\pi/100$ or exactly 100 streaks around the circumference of the cone. The streak spacing corresponds to the azimuthal wavenumber of the steady streamwise mode (0,2), which is nonlinearly generated by interaction of the forced oblique modes $(1, \pm 1)$. Farther downstream these streaks merge in the azimuthal direction resulting in an increased Stanton number around the entire circumference of the cone, indicating that the flow has progressed deep into the nonlinear breakdown regime. The development of the Stanton number in the downstream direction extracted at different azimuthal locations is displayed in figure 11(*b*), where the laminar and turbulent estimates for a sharp cone (shifted in the downstream direction to the virtual cone origin of a perfectly sharp cone) are provided for reference. The Stanton number extracted along the streaks ($\varphi = 0$, $\varphi = \pi/100$ rad) shows a rapid deviation from the laminar estimate towards the turbulent value around $x \approx 0.09$ m. The Stanton number extracted at an azimuthal location between the streaks (figure 11(*b*), $\varphi = \pi/50$ rad) exhibits a delayed deviation from the laminar value. At $x \approx 0.11$ m, the Stanton number has approached turbulent values at all azimuthal locations, and is later exceeding them ('overshoot') for some spanwise locations.

To provide a qualitative comparison to Schlieren images shown in Kennedy *et al.* (2019), contours of 'pseudo-schlieren' are plotted in the symmetry plane in figure 12. As for the instantaneous temperature disturbance contours (figure 8), the entropy-layer thickness ($\delta_S$) and the boundary-layer thickness ($\delta_{99.5}$) are also provided in figure 12. The shape of the structures in the entropy layer that was observed in the instantaneous contours of the temperature disturbance (see figure 8) can also be seen in the 'pseudo-schlieren' (figure 12). As these 'slanted' structures propagate in the downstream direction their 'tail' begins to penetrate the boundary layer (figure 12*b*). The previously 'quiet' boundary layer is then quickly contaminated with the disturbances from the entropy layer and breakdown to small scales can be observed (figure 12*d*). This is followed by a rapid transition of the boundary layer while the coherent entropy-layer structures persist even in the late stages of the laminar-turbulent transition process (figure 12*f*). The small scales observed in the contours of the magnitude of the density gradient in figure 12(*f*) again confirm that the nonlinear stages of transition have been reached, and the flow is approaching turbulence.

The question arises how far transition has progressed towards fully turbulent flow. This can be addressed by analysing the van Driest transformed velocity profiles from the time-averaged flow field for different downstream and azimuthal locations (figure 13). The viscous sublayer and the log-layer are given as reference as a black dashed line and a dash-dotted line, respectively, in figure 13. The azimuthal locations at which the profiles were extracted correspond to a location cutting through the streaks ($\varphi = 0$ rad) and
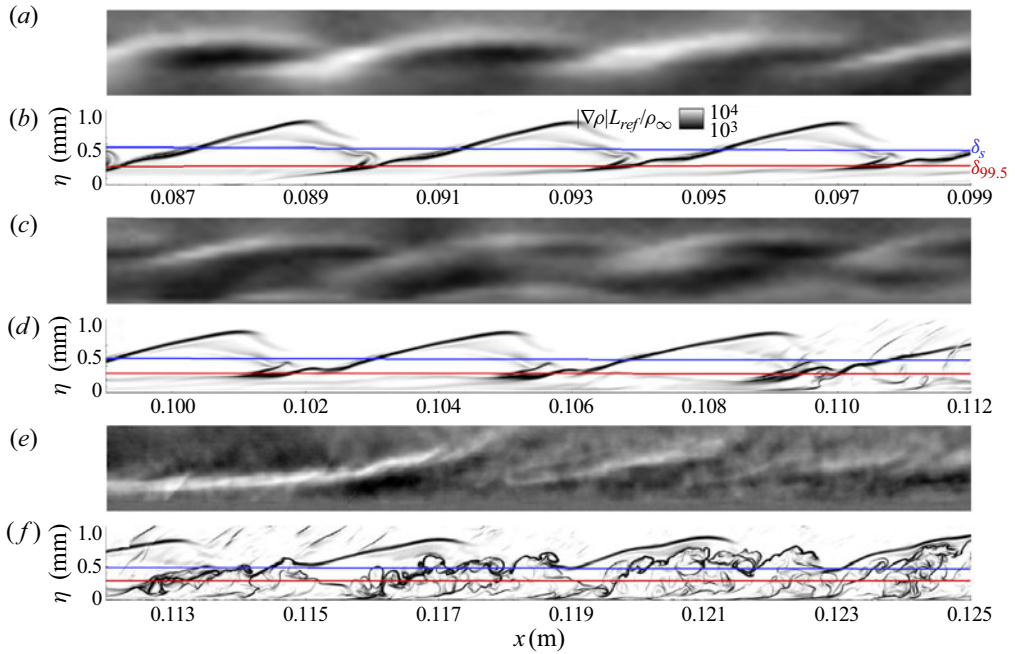
Figure 12. Qualitative comparison of the Schlieren images taken from Kennedy *et al.* (2019) (*a,c,e*) with 'pseudo-schlieren' (normalized magnitude of the density gradient, where $L_{ref} = 1$ m is the reference length scale used here) obtained from the oblique breakdown DNS (*b,d,f*).
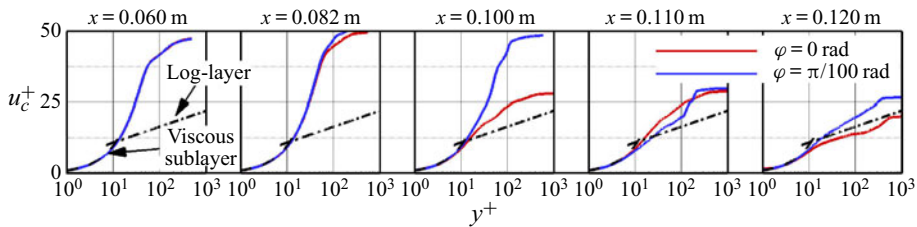


Figure 13. Van Driest transformed velocity ($u_c^+$) profiles from the oblique breakdown simulations.

between the streaks ($\varphi = \pi/100$ rad). At $x = 0.06$ m, the van Driest profiles (figure 13) at the two different azimuthal locations are indistinguishable from one another, thus the flow is most likely still laminar at this location. The profiles deviate from one another at $x = 0.082$ m (figure 13) without any noticeable development of a log-layer. The profiles in the symmetry plane begin to approach the log-layer at $x = 0.1$ m, while the profile between the streaks still appears to be laminar. Shortly downstream at $x = 0.11$ and $x = 0.12$ m (figure 13), the profiles at both azimuthal directions show the development of a log-layer, indicating that in this case the laminar-turbulent transition process is extremely rapid, resulting in a very short transition region. Here, the transition region is defined as the distance from the location where the Stanton number begins to deviate from its laminar value to where it has reached a sustained turbulent value. This rapid transition is in contrast to the findings for 'controlled' breakdown DNS for sharp straight and flared cones (see for example Laible *et al.* 2009; Hader & Fasel 2019) where the transition region covered large portions of the geometry.
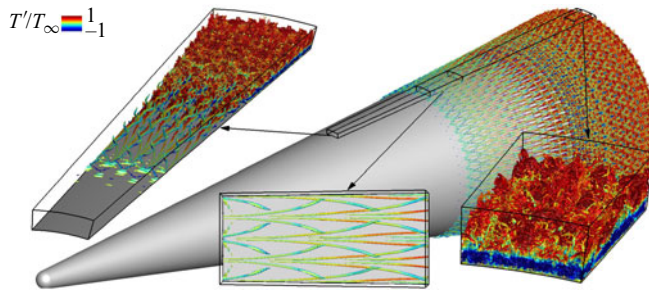
**915** R2-12

Figure 14. Instantaneous isosurfaces of $Q = 100\,000$ coloured with contours of the instantaneous temperature disturbance.

The instantaneous flow structures from the oblique breakdown simulation are visualized in figure 14 using $Q$-isocontours coloured with the contours of the instantaneous temperature disturbance. The isocontours of the $Q$-criterion confirm that the flow is laminar (no vortical structures) for a large downstream portion of the computational domain, followed by an explosive breakdown to turbulence towards the downstream end of the computational domain. The close-ups in figure 14 provide details of the laminar-turbulent breakdown process. The top down view (figure 14) shows the formation of staggered lambda vortices. At the downstream end of the computational domain, the flow has broken down to small scales, providing further evidence the boundary layer has reached the late stages of the transition process and the onset of turbulent flow.

## 7. Conclusions

Direct numerical simulations were employed to investigate the linear and nonlinear stability regimes in the entropy layer of a blunt cone at Mach 5.9. The linear stability investigations revealed that oblique waves for a wide range of frequencies and azimuthal wavenumbers experience significant growth (much larger compared with the second-mode growth rates) over a very short downstream distance in the nose region. These instabilities were not captured with conventional stability tools, such as LST, possibly due to the 'non-parallel' effects that may not be negligible in the region just downstream of the blunt nose. In spite of the very short downstream distance for which these modes are amplified, the large growth rates result in large $N$-factors (integrated growth rates). A low resolution (in azimuthal direction) onset study for the oblique breakdown showed that, due to the very large growth rates of these linear disturbances, amplitudes sufficient for a rapid nonlinear breakdown can be reached over a very short downstream distance. Thereupon, a high resolution 'controlled' oblique breakdown simulation was carried out where oblique disturbance waves were continuously, locally forced in the entropy layer at larger amplitudes, which lead to rapid transition. The results indicate that the flow has progressed deep into the nonlinear transition regime towards turbulent flow. Coherent structures were observed in the entropy layer that persisted even after the boundary layer became turbulent. Qualitative similarities of the pseudo-schlieren images from the oblique breakdown DNS presented here and the Schlieren images by Kennedy *et al.* (2019) indicate that nonlinear oblique breakdown may indeed be a relevant (nonlinear) transition mechanism in these experiments. Therefore, the results presented here provide evidence that in conventional ('noisy') wind tunnels, including the nonlinear mechanisms may be key for explaining the transition process for blunt cones.

**Author ORCIDs.**
- Andrew B. Hartman https://orcid.org/0000-0002-8264-8155;
- Christoph Hader https://orcid.org/0000-0002-0956-000X.

## REFERENCES

BERLIN, S., LUNDBLADH, A. & HENNINGSON, D. 1994 Spatial simulations of oblique transition in a boundary layer. *Phys. Fluids* **6** (6), 1949–1951.

CHAKRAVARTHY, S., PEROOMIAN, O., GOLDBERG, U. & PALANISWAMY, S. 1998 The CFD++ computational fluid dynamics software suite. *AIAA and SAE 1998 World Aviation Conference*. AIAA 1998–5564.

CHANG, C.-L. & MALIK, M.R 1994 Oblique-mode breakdown and secondary instability in supersonic boundary layers. *J. Fluid Mech.* **273**, 323–360.

DIETZ, G & HEIN, S 1999 Entropy-layer instabilities over a blunted flat plate in supersonic flow. *Phys. Fluids* **11** (1), 7–9.

FASEL, H.F., THUMM, A. & BESTEK, H. 1993 Direct numerical simulation of transition in supersonic boundary layers: oblique breakdown. In *Transitional and Turbulent Compressible Flows*, pp. 77–92. ASME-FED 151.

GROSS, A. & FASEL, H.F. 2008 High-order accurate numerical method for complex flows. *AIAA J.* **46** (1), 204–214.

HAAS, A.P. 2020 Private communication.

HADER, C. & FASEL, H.F. 2019 Direct numerical simulations of hypersonic boundary-layer transition for a flared cone: fundamental breakdown. *J. Fluid Mech.* **869**, 341–384.

HUSMEIER, F. & FASEL, H.F. 2007 Numerical investigations of hypersonic boundary layer transition for circular cones. *18th AIAA Computational Fluid Dynamics Conference*. AIAA 2007–3843.

JEWELL, J.S., KENNEDY, R.E., LAURENCE, S.J. & KIMMEL, R.L. 2018 Transition on a variable bluntness 7-degree cone at high Reynolds number. *2018 AIAA Aerospace Sciences Meeting*. AIAA 2018–1822.

JEWELL, J.S. & KIMMEL, R.L. 2016 Boundary-layer stability analysis for Stetson's mach 6 blunt-cone experiments. *J. Spacecr. Rockets*, 258–265.

KENNEDY, R.E., JAGDE, E.K., LAURENCE, S.J., JEWELL, J.S. & KIMMEL, R.L. 2019 Visualizations of hypersonic boundary-layer transition on a variable bluntness cone. In *AIAA Aviation 2019 Forum*. AIAA 2019–3079.

KLEBANOFF, P.S., TIDSTROM, K.D. & SARGENT, L.M. 1962 The three-dimensional nature of boundary-layer instability. *J. Fluid Mech.* **12** (1), 1–34.

LAIBLE, A.C., MAYER, C.S.J. & FASEL, H.F. 2009 Numerical investigation of transition for a cone at Mach 3.5: oblique breakdown. In *39th AIAA Fluid Dynamics Conference*. AIAA 2009–3557.

LEI, J. & ZHONG, X. 2012 Linear stability analysis of nose bluntness effcts on hypersonic boundary layer transition. *J. Spacecr. Rockets*, 24–37.

MACK, L.M. 1969 Boundary-layer stability theory. *Jet Propulsion Laboratory*, *NASA CR-131501*.

MARINEAU, E.C., MORARU, G.C., LEWIS, D.R., NORRIS, J.D., LAFFERTY, J.F., WAGNILD, R.M. & SMITH, J.A. 2014 Mach 10 boundary layer transition experiments on sharp and blunted cones. *19th AIAA International Space Planes and Hypersonic Systems and Technologies Conference*. AIAA 2014–3108.

MAYER, C.S.J., VON TERZI, D.A. & FASEL, H.F. 2011*a* Direct numerical simulation of complete transition to turbulence via oblique breakdown at Mach 3. *J. Fluid Mech.* **674**, 5–42.

MAYER, C.S.J., WERNZ, S. & FASEL, H.F. 2011*b* Numerical investigation of the nonlinear transition regime in a Mach 2 boundary layer. *J. Fluid Mech.* **668**, 113–149.

PAREDES, P., CHOUDHARI, M.M. & LI, F. 2019*a* Laminar-turbulent transition upstream of the entropy-layer swallowing location in hypersonic boundary layers. *AIAA Aviation 2019 Forum*. AIAA 2019–3215.

PAREDES, P., CHOUDHARI, M.M., LI, F., JEWELL, J.S. & KIMMEL, R.L. 2019*b* Nonmodal growth of traveling waves on blunt cones at hypersonic speeds. *AIAA Journal* **57** (11), 4738–4749.

**915** R2-14

ROSENBOOM, I., HEIN, S. & DALLMANN, U. 2013 Influence of nose bluntness on boundary-layer instabilities in hypersonic cone flows. *30th Fluid Dynamics Conference. AIAA* 2013-3591.

SCHUBAUER, G.B. & SKRAMSTAD, H.K. 1948 Laminar boundary layer oscillations and transition on a flat plate. *NASA Rep.* 909.

STETSON, K. 1979 Effect of bluntness and angle of attack on boundary layer transition on cones and biconic configurations. In *17th Aerospace Sciences Meeting*. AIAA 1979–0269.

STETSON, K. 1983 Nosetip bluntness effects on cone frustum boundary layer transition in hypersonic flow. *16th Fluid and Plasmadynamics Conference. AIAA* 1983-1763.

WHITE, F.M. 2006 *Viscous Fluid Flow*, International edn. McGraw-Hill.